Research Square

Preprints are preliminary reports that have not undergone peer review.
They should not be considered conclusive, used to inform clinical practice,
or referenced by the media as validated information.

NUS-8-Confined CsPbBr3 Nanocrystals with Enhanced Photoluminescence and Ambient Stability through Ligand-Free Mechanosynthesis

Jingru Zhang

jingruzhang@sust.edu.cn

Shaanxi University of Science and Technology Xi\'an Campus: Shaanxi University of Science and Technology https://orcid.org/0000-0002-4923-0208

Lisha Xie

Shaanxi University of Science and Technology Xi\'an Campus: Shaanxi University of Science and Technology

Hongxing Xu

Zhongcheng Valve Group Co., Ltd

Jialong Xing

Shaanxi University of Science and Technology Xi\'an Campus: Shaanxi University of Science and Technology

Weihong Xu

Shaanxi University of Science and Technology Xi\'an Campus: Shaanxi University of Science and Technology

Tianfei Xu

Shaanxi University of Science and Technology

Shengzhong (Frank) Liu

Dalian Institute of Chemical Physics, University of Chinese Academy of Sciences https://orcid.org/0000-0002-6338-852X

Article

Keywords: CsPbBr3 nanocrystals, Metal-organic frameworks, Mechanochemical synthesis, Photoluminescence, Stability

Posted Date: November 20th, 2026

DOI: https://doi.org/10.21203/rs.3.rs-11673423/v1

License: This work is licensed under a Creative Commons Attribution 4.0 International License.
Read Full License

Additional Declarations: There is a conflict of interest

NUS-8-Confined $CsPbBr_3$ Nanocrystals with Enhanced Photoluminescence and Ambient Stability through Ligand-Free Mechanosynthesis

Jingru Zhang,[*1] Lisha Xie,[1] Hongxing Xu,[2] Jialong Xing,[1] Weihong Xu,[1] Tianfei Xu[*1] and Shengzhong (Frank) Liu[*3,4]

1. College of Bioresources Chemical and Materials Engineering，Shaanxi University of Science & Technology, 6, Xuefu Road, Xi'an, 710021, P.R. China.

2. Zhongcheng Valve Group Co., Ltd.No.102, Dayuan Street, Lishui City, Zhejiang Province, 325105, PR. China

3. Key Laboratory of Photoelectric Conversion and Utilization of Solar Energy, Dalian Institute of Chemical Physics; Center of Materials Science and Optoelectronics Engineering, University of Chinese Academy of Sciences, Beijing,100049, P. R. China.

4. School of Materials Science Engineering, Shaanxi Normal University, Xi'an, Shaanxi 710119, China

* Corresponding authors

E-mail address: jingruzhang@sust.edu.cn, xutf@sust.edu.cn, szliu@dicp.ac.cn

Abstract: $CsPbBr_3$ perovskite quantum dots (PQDs) are promising emitters for lighting and displays, but uncontrolled growth, surface defects, and environmental degradation limit their practical use. Herein, we report a multifunctional confined nanoreactor strategy that combines spatial confinement with interfacial defect regulation to simultaneously control the nucleation and photoluminescence stability of $CsPbBr_3$ PQDs. NUS-8, a two-dimensional Zr-based MOF with mesoporous channels and abundant carboxyl sites, serves as the host to confine PQD formation through chemical interactions. A ligand-free mechanochemical method is used to trigger the in-situ nucleation of $CsPbBr_3$ QDs within the nanospace of NUS-8, yielding uniformly confined nanocrystals of approximately 3-5 nm. The nanospace of NUS-8 regulates crystal growth by restricting particle migration, while coordination between carboxyl groups and Pb^{2+} reconstructs the interfacial electronic environment and inhibits trap-assisted non-radiative recombination. The optimized $CsPbBr_3$@NUS-8 composite exhibits a photoluminescence quantum yield of 55% and an average lifetime of 170.9 ns, demonstrating effective suppression of defect-mediated recombination. The $CsPbBr_3$@NUS-8 composite retains ~85% of its initial PL intensity after 50 days of storage in air and ~72% after 168 h of continuous UV irradiation. In addition, the composite can be used for white LED fabrication and fluorescent patterning, demonstrating its potential for stable optoelectronic devices.

Key words: $CsPbBr_3$ nanocrystals; Metal-organic frameworks; Mechanochemical synthesis; Photoluminescence; Stability

1. Introduction

All-inorganic $CsPbBr_3$ perovskite quantum dots (PQDs) have advantages such as tunable emission wavelength, high color purity and excellent photophysical properties, and have become popular candidate materials in the field of optoelectronic device applications. However, the intrinsic instability caused by uncontrollable nucleation/growth, surface defects and ion migration severely limits their practical applications. In particular, the defect-rich surface of $CsPbBr_3$ PQDs will generate trap states, accelerate non-radiative recombination, and cause irreversible degradation under environmental stress [1-8]. For example, insufficiently coordinated Pb^{2+} sites, halogen vacancies, migration-induced defects, etc. will introduce non-radiative recombination centers, leading to rapid photoluminescence quenching and poor luminescence durability [9]. Therefore, simultaneously inhibiting structural degradation and defect-mediated non-radiative recombination is the key to promoting the practical optoelectronic device application of $CsPbX_3$ PQDs.

At present, researchers have developed a variety of strategies to improve the stability of $CsPbBr_3$ PQDs, including surface ligand engineering, inorganic encapsulation, polymer protection, etc. Surface ligands can effectively coordinate with insufficiently coordinated surface ions, reduce defect-assisted recombination, and thus improve photoluminescence performance[10-12]. However, the dynamic binding characteristics of organic ligands and their easy desorption during long-term operation will damage the structural integrity and stability of PQDs. In addition to surface ligand modification, ion doping with metal cations or anions is also an effective method to regulate the crystal lattice, reduce defect density and inhibit ion migration[13, 14]. However, lattice engineering alone is not enough to prevent the agglomeration of nanoparticles, nor can it solve the long-term degradation problem caused by external environmental factors. In addition, inorganic shells and polymer matrices can form physical barriers against moisture, oxygen and other environmental factors, for example, quantum dots are encapsulated in inorganic shells such as SiO_2, Al_2O_3 or organic-inorganic hybrid networks[15-19], or embedded in polymer matrices or inorganic glass hosts[20-22]. However, these methods mainly focus on external protection, and have limited regulatory effects on the nucleation and growth behavior of quantum dots and the interfacial electronic structure. Therefore, there is an urgent need for an advanced stabilization strategy that can not only regulate the structure during the formation of PQDs, but also chemically regulate the surface defects.

Metal-organic frameworks (MOFs) have the characteristics of high specific surface area, tunable pore structure and abundant functional groups, and have become a promising platform for regulating the nucleation, growth and surface chemical properties of perovskite quantum dots (PQDs)[23-33]. The confined nanospace inside the MOF skeleton can effectively limit the migration and agglomeration of PQDs, thus realizing the controllable regulation of crystal growth and improving environmental stability.

For example, Zhao et al. encapsulated $CsPbX_3$ quantum dots inside ZIF-8 through a mechanical grinding strategy, and the obtained $CsPbBr_3$/ZIF-8 composite still retained about 80% of its initial photoluminescence intensity after being stored at room temperature for 75 days [34]. Similarly, Ren et al. introduced $CsPbBr_3$ quantum dots into mesoporous MOF-5, which improved the thermal stress resistance and UV irradiation resistance of the material[35]. In addition to physical confinement, functionalized MOFs with abundant coordination sites can also regulate the interfacial properties of PQDs. For example, existing studies have reported that carboxyl-rich MOFs such as Cu-BTC and UiO-66 can improve the photoluminescence intensity and humidity stability of perovskite quantum dots by enhancing host-guest interaction[24, 36-39]. However, most of the currently reported MOF-based strategies still mainly rely on physical confinement, and MOFs mainly act as passive barriers against external degradation factors. Research on the synergistic regulation of PQDs nucleation, crystal growth and interfacial defect chemistry through a MOF environment with chemical interaction still needs to be further deepened. Therefore, developing a multifunctional MOF host combining spatial confinement and interfacial defect regulation functions is a promising strategy for preparing $CsPbBr_3$ PQDs with high stability and high efficiency.

NUS-8 is a two-dimensional Zr-based MOF constructed by Zr_6 clusters and H_3BTB tricarboxylic acid linkers[40, 41]. Its hierarchical micro/mesoporous structure (especially the mesopores of 3~10 nm) can provide suitable nanoscale confined space for regulating the nucleation and growth of $CsPbBr_3$ QDs, and inhibit uncontrollable agglomeration at the same time. In addition, the abundant carboxyl groups in NUS-8 can provide coordination sites to interact with insufficiently coordinated Pb^{2+} species on the surface of PQDs, thereby reducing Pb-related trap states and inhibiting defect-assisted non-radiative recombination. At the same time, the robust Zr_6 cluster skeleton and stable carboxylic acid coordination network endow NUS-8 with excellent structural integrity, which is conducive to maintaining the confined environment during the formation and long-term operation of PQDs. Therefore, NUS-8 is an ideal multifunctional host integrating physical confinement and PQDs interfacial chemical regulation functions.

This study reports a ligand-free mechanochemical strategy, which can grow $CsPbBr_3$ QDs in situ in the carboxyl-rich NUS-8 skeleton. NUS-8 is not used as a passive encapsulation matrix, but as a multifunctional nanoreactor: its confined nanospace can regulate the nucleation and growth of PQDs, while the carboxyl groups can have chemical interaction with insufficiently coordinated Pb^{2+} sites, inhibiting interfacial defects and trap-assisted recombination. Benefiting from the synergistic effect of spatial confinement and interfacial defect regulation, the optimized $CsPbBr_3$@NUS-8 composite has a PLQY of up to 55% and an average photoluminescence lifetime of 170.9 ns. In addition, $CsPbBr_3$@NUS-8 still retains 85% of its initial PL intensity after being stored in air for 50 days, and maintains 72% of its emission intensity after 144 h of continuous UV irradiation. The composite can also be used for white

LED preparation and fluorescent patterning, which proves its application potential in the fields of stable optoelectronic devices and information-related fields. This work proposes a strategy based on multifunctional MOF, which can simultaneously regulate the growth of PQDs and interfacial defect chemistry, and provides a new way for the preparation of high-stability perovskite quantum dots.

2. Results and Discussion

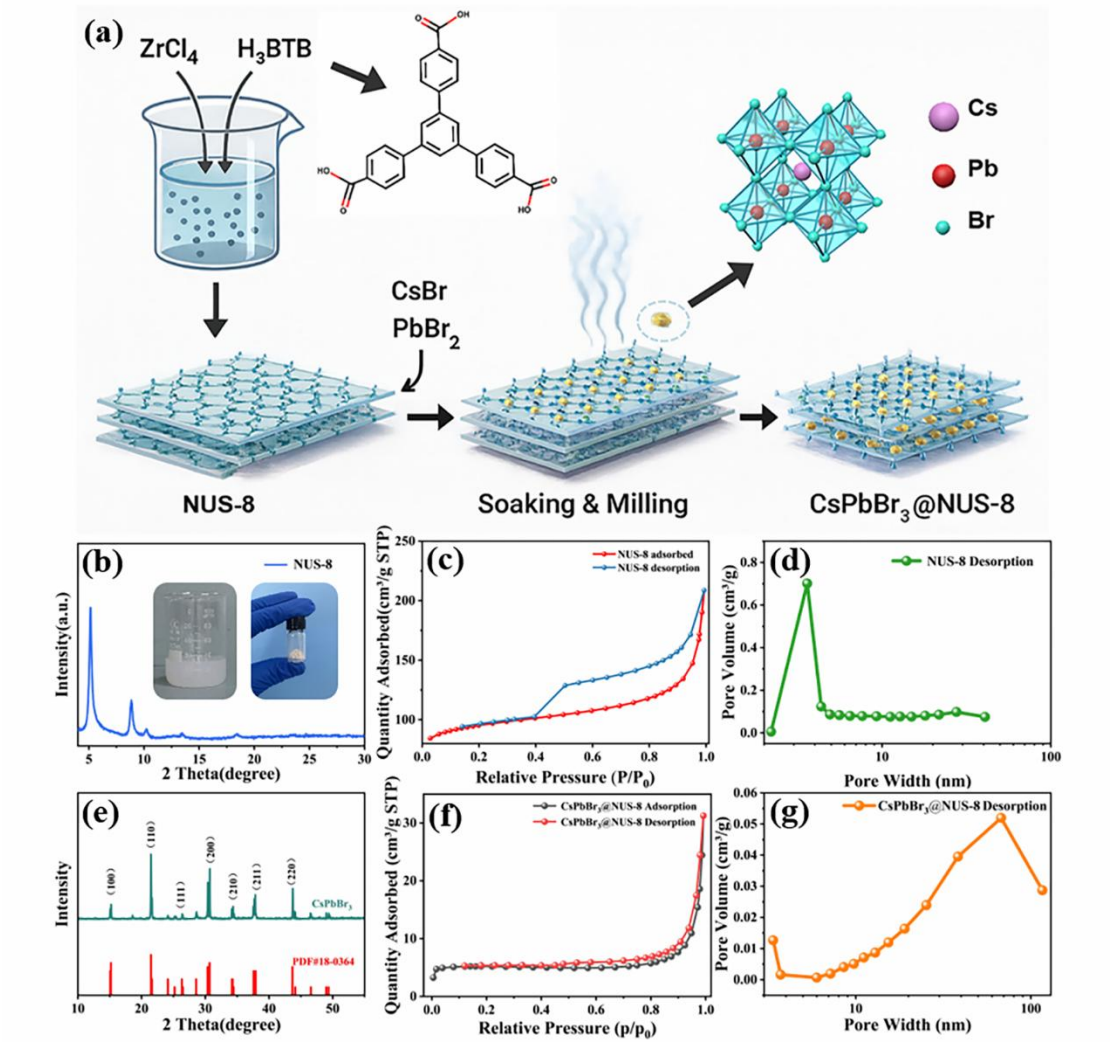


Figure 1. (a) Schematic illustration of the synthesis route for NUS-8 and the preparation of $CsPbBr_3$@NUS-8 composite quantum dots; (b) XRD pattern of NUS-8 powder (inset: photographs of NUS-8 in liquid and solid states); (c) N_2 adsorption-desorption isotherms of NUS-8; (d) pore-size distribution of NUS-8; (e) XRD pattern of $CsPbBr_3$ and comparison with the standard $CsPbBr_3$ card (PDF#18-0364); (f) N_2 adsorption-desorption isotherms of $CsPbBr_3$@NUS-8; (g) pore-size distribution of $CsPbBr_3$@NUS-8.

Figure 1a shows the synthesis strategy of the NUS-8 confined nanoreactor and the in-situ formation process of $CsPbBr_3$ quantum dots in its nanoscale channels. First, NUS-8 is synthesized through the solvothermal coordination reaction of $ZrCl_4$ and H_3BTB in the DMF/H_2O/formic acid system, and a two-dimensional layered skeleton with hierarchical micro/mesoporous channels is obtained. Then CsBr and

NUS-8 powder are fully ground in a mortar, so that Cs+ ions are pre-distributed in the skeleton channels and interlayer gaps. Then $PbBr_2$ is added for further grinding to trigger the in-situ formation of $CsPbBr_3$ quantum dots in the channels of NUS-8, and finally $CsPbBr_3$@NUS-8 composite powder is obtained. Figure 1b is the X-ray diffraction (XRD) pattern of NUS-8 powder, and its characteristic diffraction peaks are in good agreement with the characteristic peaks of NUS-8 reported in the literature, which proves that the characteristic layered crystal structure of NUS-8 is retained. The inset is the photos of dispersed and powdered NUS-8, and its suspension is milky white, which further proves that it has good dispersibility. As shown in the XRD pattern of Figure 1e, the diffraction peaks of pure $CsPbBr_3$ quantum dots at 15.2°, 21.5°, 26.4°, 30.5°, 34.4°, 37.9°, 43.8° can be attributed to the (100), (110), (111), (200), (210), (211) and (220) crystal planes of cubic phase $CsPbBr_3$ respectively. These peaks are in good agreement with the standard PDF card of cubic phase $CsPbBr_3$ perovskite [42], which proves that the mechanochemical process can synthesize $CsPbBr_3$ quantum dots with cubic perovskite structure. To explore the regulatory effect of NUS-8 nanospace on the growth of $CsPbBr_3$, N_2 adsorption-desorption test (Brunauer-Emmett-Teller (BET) analysis) was carried out. Figure 1c is the N_2 adsorption-desorption isotherm of NUS-8, which presents the characteristics of type IV isotherm with H3 hysteresis loop, proving that NUS-8 has hierarchical porous characteristics and can provide a confined environment for precursor diffusion and quantum dot growth [43, 44]. The corresponding BJH pore size distribution (Figure 1d) has a sharp peak at about 3 nm, indicating that pores in this size range contribute the most to the pore volume, which is consistent with its layered micro/mesoporous structure. After introducing $CsPbBr_3$, the total adsorption capacity of the N_2 adsorption-desorption isotherm (Figure 1f) of $CsPbBr_3$@NUS-8 composite powder is significantly reduced compared with that of pure NUS-8, showing the characteristics of type II isotherm, the adsorption capacity rises rapidly in the low-pressure region, and the adsorption-desorption branches almost coincide, indicating that the mesoporous part has been occupied by $CsPbBr_3$ quantum dots. The corresponding pore size distribution (Figure 1g) shows that the original pore volume peak concentrated at about 3 nm is significantly weakened, and a new mesoporous distribution appears in the range of 10~50 nm. This change can be attributed to the deposition of $CsPbBr_3$ quantum dots on the surface of nanosheets and near the pore openings. As summarized in Table S1, the BET specific surface area decreases from about 300 $m^2 g^{-1}$ to 20.89 $m^2 g^{-1}$, and the mesoporous and microporous volumes decrease from 0.2019 $cm^3 g^{-1}$ and 0.119 $cm^3 g^{-1}$ to 0.048 $cm^3 g^{-1}$ and 0.082 $cm^3 g^{-1}$ respectively, confirming that $CsPbBr_3$ has been successfully loaded into the NUS-8 skeleton.

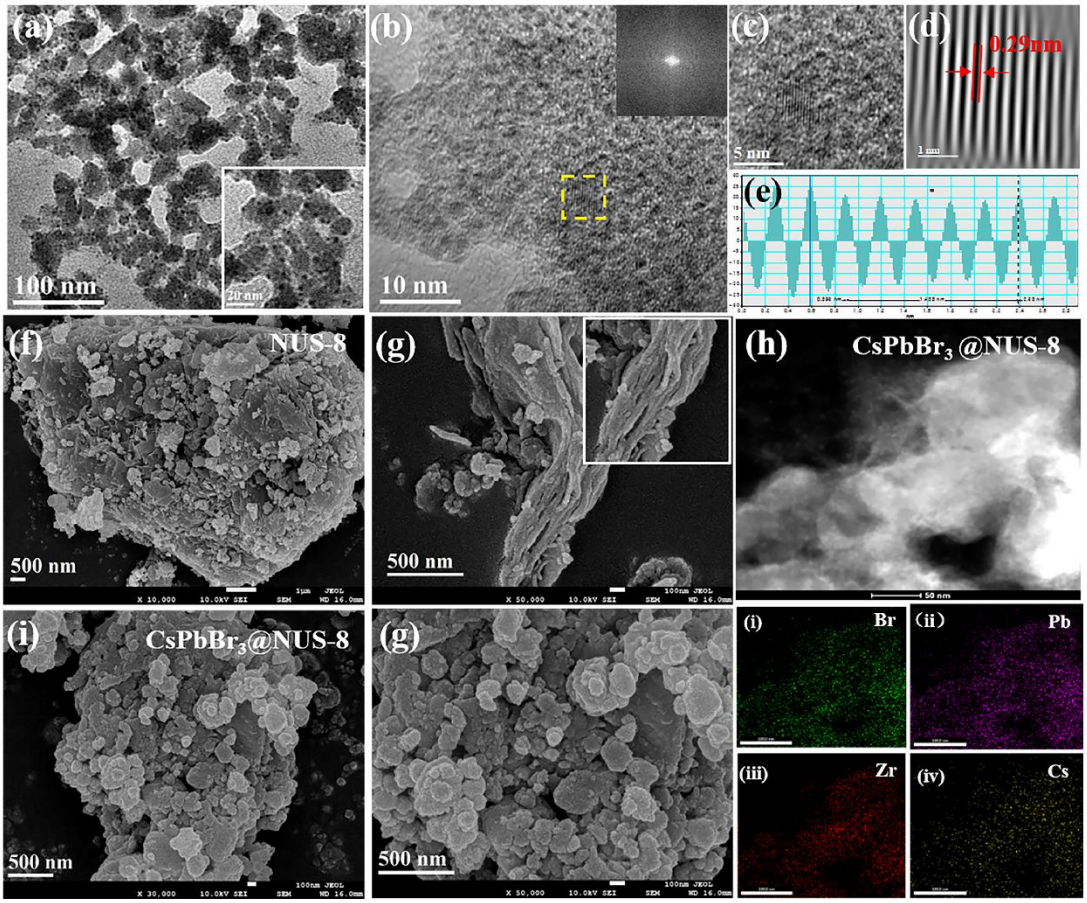


Figure 2. (a) TEM image of pristine $CsPbBr_3$ quantum dots (inset: enlarged high-magnification view); (b) TEM image of the $CsPbBr_3$@NUS-8 composite and the corresponding selected-area electron diffraction (SAED) pattern; (c) high-resolution TEM (HRTEM) image of $CsPbBr_3$@NUS-8; (d) magnified view of $CsPbBr_3$ lattice fringes with the interplanar spacing labeled; (e) intensity profile along the lattice-fringe direction; (f, g) SEM images of NUS-8 at different magnifications; (h) EDS mapping image of the $CsPbBr_3$@NUS-8 composite; (i, j) SEM images of the $CsPbBr_3$@NUS-8 composite at different magnifications; (k-n) SEM elemental mapping images of $CsPbBr_3$@NUS-8.

To explore the microstructure characteristics and spatial distribution of $CsPbBr_3$ quantum dots inside the NUS-8 skeleton, transmission electron microscope (TEM) test was carried out on the $CsPbBr_3$@NUS-8 composite powder (Figure 2a). The TEM image shows that $CsPbBr_3$ QDs are uniformly distributed in the flaky NUS-8 skeleton without obvious agglomeration, and the average size of $CsPbBr_3$ QDs is measured to be 4.4 nm (Figure S2), which proves that the nanoconfinement effect provided by NUS-8 effectively limits uncontrollable crystal growth. The magnified high-resolution TEM image and the corresponding fast Fourier transform (FFT) inset (Figure 2b) show that the quantum dots have clear and ordered lattice fringes with a crystal plane spacing of about 0.29 nm, which can be attributed to the (200) crystal plane of cubic phase $CsPbBr_3$, confirming that the obtained nanocrystals have high crystallinity[27]. The scanning electron microscope (SEM) images of NUS-8 and CsPbBr3@NUS-8 are shown in Figure 2f and 2g. Pure NUS-8 presents irregular bulk particles

agglomerated by nanosheets, which is consistent with the morphology of its layered skeleton.

After the in-situ growth of $CsPbBr_3$ QDs, the overall morphology of $CsPbBr_3$@NUS-8 composite particles still remains irregular bulk (Figure 2g-i), indicating that the NUS-8 skeleton maintains structural integrity during the mechanochemical treatment process. However, its surface changes from a relatively smooth layered texture to a rough morphology composed of a large number of fine particles, indicating that the quantum dots are uniformly dispersed and anchored on the outer surface and inside the channels of the NUS-8 skeleton, and no large agglomerates are formed. To verify this uniform dispersibility, the elemental composition and spatial distribution were tested. The EDS mapping image (Figure 2h) shows that the Br, Pb, Cs signals and Zr signal are highly co-localized in the whole particle region, confirming that $CsPbBr_3$ quantum dots are uniformly distributed inside and on the surface of NUS-8 particles.

To regulate the formation of $CsPbBr_3$ QDs and optimize their optical properties, the effect of precursor stoichiometric ratio on the structure and photoluminescence behavior of $CsPbBr_3$@NUS-8 composites was systematically explored. $CsPbBr_3$@NUS-8 composites with different CsBr:$PbBr_2$ molar ratios were prepared by changing the precursor feeding ratio. The XRD patterns (Figure S3) show that in the range of 0.5:1~1.5:1, all samples present the characteristic diffraction peaks of $CsPbBr_3$, the peak positions are basically the same, and only the peak intensity and peak width have slight differences. In addition, the characteristic vibration peaks of NUS-8 in the FTIR spectra (Figure S4) remain almost unchanged, indicating that the NUS-8 skeleton maintains structural integrity under different precursor ratios. When the CsBr:$PbBr_2$ ratio is 1:1, the PL intensity reaches the maximum value (Figure S5), and the emission peak has a relative blue shift, indicating that under this optimized stoichiometric ratio condition, defect-related recombination is reduced, which is more conducive to the formation of $CsPbBr_3$ QDs with high emission performance.

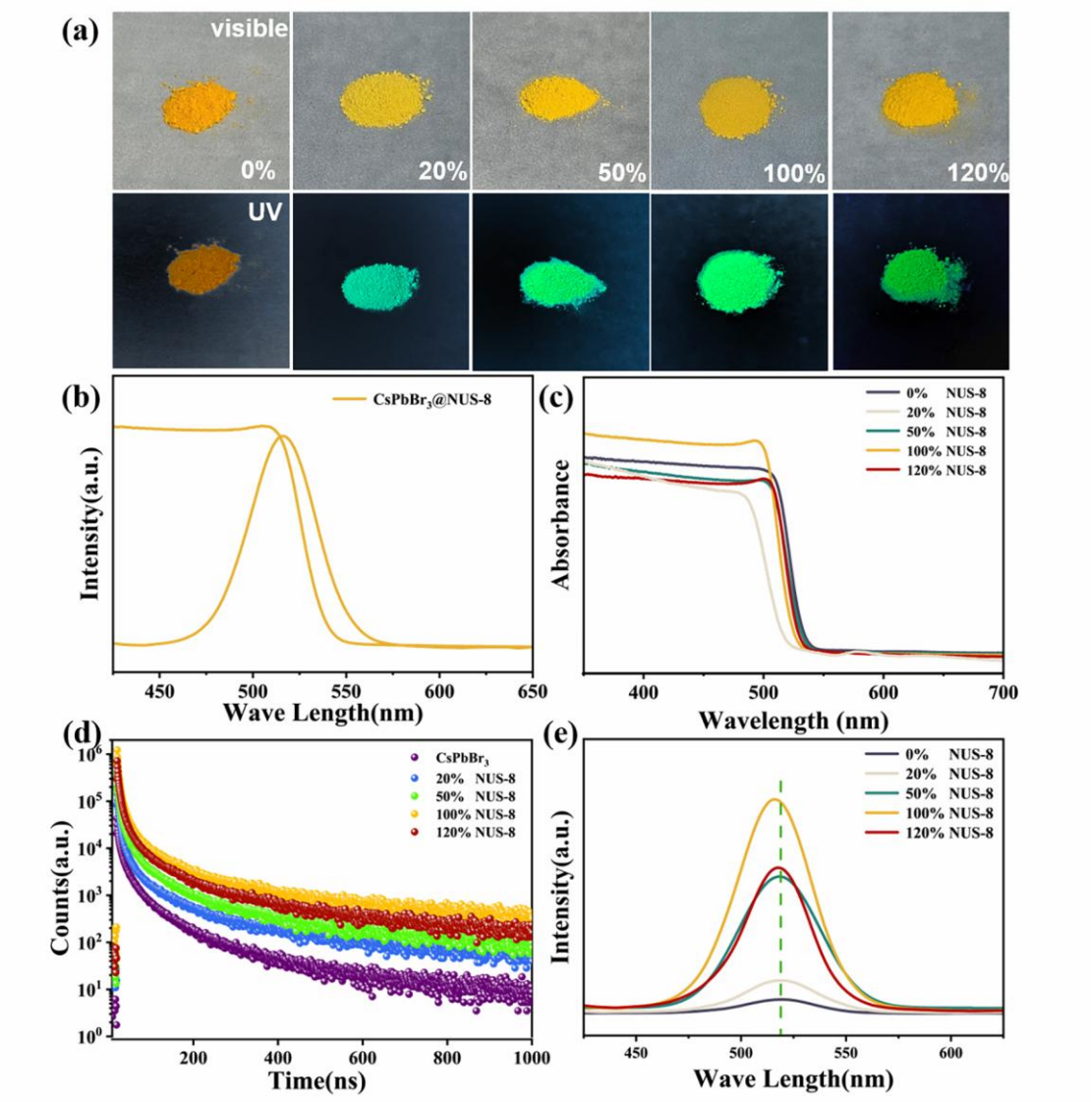


Figure 3. (a) Photographs of $CsPbBr_3$@NUS-8 composite powders with different NUS-8 contents (0%, 20%, 50%, 100%, and 120%) under visible light and 365 nm UV irradiation; (b) UV-vis absorption and photoluminescence (PL) emission spectra of the $CsPbBr_3$@NUS-8 composite powder; (c) UV-vis absorption spectra of $CsPbBr_3$@NUS-8 composite powders with different NUS-8 contents; (d) time-resolved photoluminescence decay curves of $CsPbBr_3$@NUS-8 composite powders with different NUS-8 contents; (e) steady-state PL emission spectra of $CsPbBr_3$@NUS-8 composite powders with different NUS-8 contents (with pristine $CsPbBr_3$ as a reference).

Subsequently, on the basis of optimizing the precursor ratio, the addition amount of NUS-8 was changed to further explore the effect of component ratio on the luminescence performance of $CsPbBr_3$@NUS-8. As shown in Figure 3a, under visible light irradiation, $CsPbBr_3$@NUS-8 composite powders with different NUS-8 contents are all orange-yellow. In contrast, under 365 nm UV excitation, pure $CsPbBr_3$ powder without NUS-8 has almost no emission. With the increase of NUS-8 content, the green fluorescence increases significantly, and reaches the maximum when the NUS-8 loading is 100%, indicating that an appropriate amount of NUS-8 is conducive to improving the emission efficiency of

$CsPbBr_3$ QDs. But when the NUS-8 content is further increased to 120%, the fluorescence intensity decreases slightly. This decrease may be attributed to the agglomeration of thick stacked layers and the occurrence of "emission self-absorption" phenomenon [45]: part of the ultraviolet light is absorbed by the material, and the scattering and shielding effects during the emission process cause part of the luminescence to be blocked or reabsorbed, thereby reducing the photoluminescence (PL) output.

Table 1 TRPL fitting parameters of $CsPbBr_3$@NUS-8 composite powders prepared with different NUS-8 contents

Sample	τ_1 /ns	A_1/%	τ_2/ns	A_2/%	τ_3/ns	A_3/%	τ_{av}/ns
$CsPbBr_3$	298.5	14.49	54.25	49.37	11.36	36.15	74.1
20%NUS-8@PQDs	528.7	19.77	71.72	44.47	12.86	35.76	141
50%NUS-8@PQDs	513.6	23.69	72.92	45.06	11.90	31.26	158.2
100%NUS-8@PQDs	568.8	23.51	76.18	43.64	12.04	32.85	170.9
120%NUS-8@PQDs	534.7	22.25	80.95	46.88	14.81	30.87	161.5

In addition, Figure 3d shows the time-resolved photoluminescence (TRPL) decay curves of pure $CsPbBr_3$ and $CsPbBr_3$@NUS-8 composite powders with different NUS-8 contents. Compared with pure $CsPbBr_3$ powder, the average lifetime of the composite powder prolongs with the increase of NUS-8 content, and reaches the maximum value (τ_{av} = 170.9 ns) when the NUS-8 loading is 100%, indicating that an appropriate amount of NUS-8 framework can inhibit defect-assisted non-radiative recombination in $CsPbBr_3$ quantum dots (QDs). On the one hand, MOF pores can provide spatial confinement effect, thereby inhibiting quantum dot aggregation and ion migration. On the other hand, oxygen-containing coordination groups in ligands and frameworks can interact with defect sites such as coordinatively unsaturated surface Pb^{2+}, thereby reducing the probability of non-radiative recombination. When the NUS-8 content is too high, the average lifetime of the composite decreases slightly (τ_{av} = 161.5 ns), which is attributed to the light absorption and scattering effects caused by excessive NUS-8[46]. The PL decay curves are fitted with a tri-exponential decay function:

$$A(t) = A_1 \exp\left(-\frac{t}{\tau_1}\right) + A_2 \exp\left(-\frac{t}{\tau_2}\right) + A_3 \exp\left(-\frac{t}{\tau_3}\right)$$

Figure 3e shows the photoluminescence intensities of composite powders with different NUS-8 loadings. The emission intensity of pure phase $CsPbBr_3$ quantum dots is the lowest. The PL intensity increases significantly with the increase of NUS-8 content, reaches the maximum when the NUS-8 loading is 100%, with a corresponding PLQY of 55% (Figure S6), and decreases slightly when the loading rises to 120%. This change trend is consistent with the optical photos of the powders under ultraviolet irradiation in Figure 3a. In addition, after the introduction of NUS-8, the emission peak of the $CsPbBr_3$ quantum dot composite powder shows a slight blue shift, which is jointly caused by the quantum confinement effect of the NUS-8 framework and the passivation of undercoordinated Pb^{2+} defects on the

surface of the quantum dots.

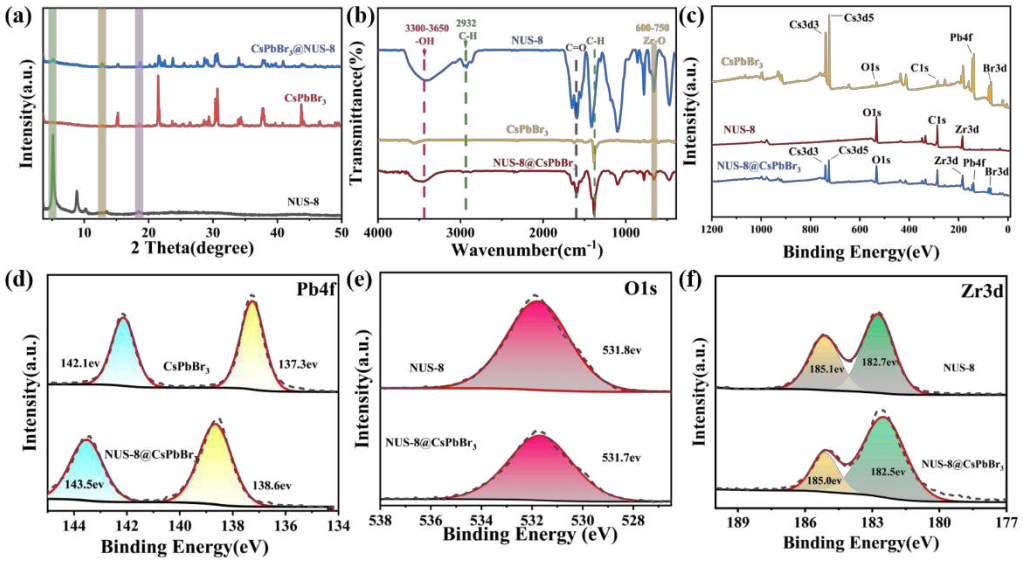


Figure 4. (a) Comparison of XRD patterns of NUS-8, $CsPbBr_3$, and $CsPbBr_3$@NUS-8 composite powders; (b) Fourier-transform infrared (FTIR) spectra of NUS-8, $CsPbBr_3$, and $CsPbBr_3$@NUS-8; (c) XPS survey spectra of NUS-8, $CsPbBr_3$, and $CsPbBr_3$@NUS-8; (d) high-resolution Pb 4f XPS spectra of pristine $CsPbBr_3$ and $CsPbBr_3$@NUS-8; (e) high-resolution O 1s XPS spectra of pristine NUS-8 and $CsPbBr_3$@NUS-8; (f) high-resolution Zr 3d XPS spectra of pristine NUS-8 and $CsPbBr_3$@NUS-8.

As shown in Figure 4a, the diffraction peaks of the $CsPbBr_3$@NUS-8 composite powder in the XRD pattern correspond one-to-one with the characteristic diffraction peaks of pure phase NUS-8 and $CsPbBr_3$. The framework diffraction peaks of NUS-8 are located in the low-angle region near 7.4° and 8.6°, and the main diffraction peaks of $CsPbBr_3$ appear around 15.2°, 21.5° and 30.5°. All the above diffraction peaks are retained in the composite powder, and no obvious new impurity phase peaks are observed, indicating that $CsPbBr_3$ has been successfully loaded into the NUS-8 framework, and the crystal structure of the host framework is not destroyed.

The FTIR spectrum of Figure 4b also provides key evidence. The O-H characteristic stretching vibration band of NUS-8 is in the range of 3300~3650 cm^{-1}, the C-H stretching vibration band is at about 2932 cm^{-1}, and the C=O stretching vibration band appears near about 1600 cm^{-1}. The composite powder basically retains all the above characteristic bands, but the C=O and Zr-O bands show a slight shift (about 5~10 cm^{-1}), indicating that there is an interfacial interaction between $CsPbBr_3$ and the functional groups in the pores of NUS-8.

Subsequently, X-ray photoelectron spectroscopy (XPS) was used to analyze the surface chemical state and element composition of the composite powder. As shown in Figure 4c and Figures S7~S9, clear characteristic peaks of Cs, O, C, Zr, Br and Pb can be observed in the XPS spectrum, confirming the existence of the above elements in the composite powder. As shown in Figure 4d, the peaks at 143.52 eV and 138.65 eV correspond to the Pb 4f 5/2 and Pb 4f 7/2 signals of $CsPbBr_3$ quantum dots in the

$CsPbBr_3$@NUS-8 composite, respectively. Compared with pure phase $CsPbBr_3$, these two peaks obviously shift to the direction of high binding energy, indicating that there is a strong interfacial interaction between the Pb^{2+} species on the surface of $CsPbBr_3$ and the ligands of NUS-8. As can be seen from Figure 4f, the Zr 3d 5/2 and Zr 3d 3/2 peaks are located at 182.5 eV and 185.11 eV respectively, both slightly shifting to the direction of low binding energy compared with pure phase NUS-8. The O 1s peak in Figure 4e also shows the same change trend. The peaks at 738.1 eV and 724.2 eV are attributed to the Cs 3d 3/2 and Cs 3d 5/2 energy levels of $CsPbBr_3$ in the $CsPbBr_3$@NUS-8 composite, which also shift to the direction of high binding energy; the peaks at 68 eV and 69.1 eV correspond to the Br 3d 5/2 and Br 3d 3/2 signals of $CsPbBr_3$ in the composite. The above binding energy shift phenomena jointly prove that there is chemical interaction at the interface, which further verifies the feasibility of the NUS-8 framework as a carrier for $CsPbBr_3$ quantum dots.

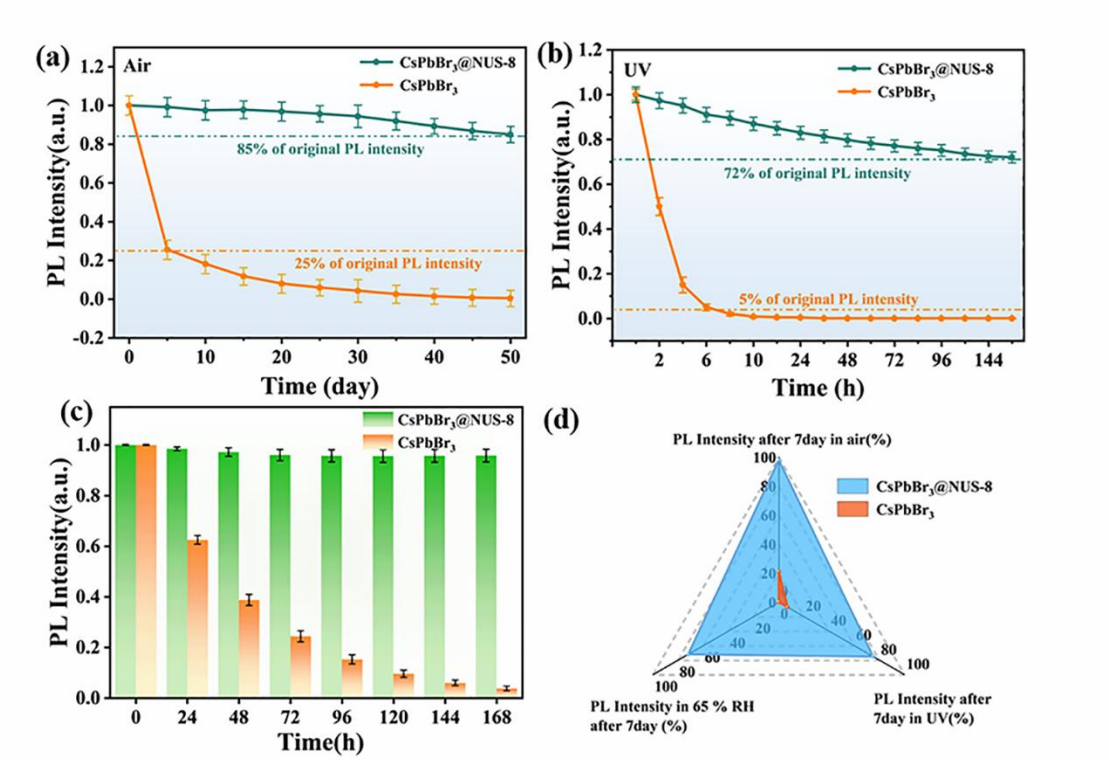


Figure 5. (a) PL intensity evolution of pristine $CsPbBr_3$ quantum dots and $CsPbBr_3$@NUS-8 composite powder as a function of storage time in air; (b) PL intensity evolution of pristine $CsPbBr_3$ and $CsPbBr_3$@NUS-8 under continuous UV irradiation; (c) bar-chart comparison of PL intensity evolution of pristine $CsPbBr_3$ and $CsPbBr_3$@NUS-8 over time at 65% relative humidity; (d) radar-plot statistics of PL intensity retention for $CsPbBr_3$ and $CsPbBr_3$@NUS-8 after 7 days under three conditions: air, UV irradiation, and 65% relative humidity.

To explore the effect of NUS-8 on the stability of $CsPbBr_3$ quantum dots, the change rules of photoluminescence (PL) intensity of $CsPbBr_3$ quantum dot powder and $CsPbBr_3$@NUS-8 composite in different environments were compared. As shown in Figure 5a, in the air environment (24℃, relative

humidity 40%), the PL intensity of pure phase $CsPbBr_3$ rapidly drops to about 25% of the initial value within 5 days; while the $CsPbBr_3$@NUS-8 compᵒsite can still retain about 85% of the initial PL intensity after 50 days, indicating that the NUS-8 framework can effectively inhibit the degradation of the material under environmental conditions. The reason for the improved stability is that the confined pore structure of NUS-8 can block the intrusion of water vapor and oxygen, and reduce the contact between $CsPbBr_3$ quantum dots and external degradation factors. Figure 5b compares the stability of the two materials under ultraviolet irradiation: the PL intensity of pure phase $CsPbBr_3$ drops to 5% of the initial value within 7 hours, because ultraviolet irradiation will accelerate the surface and lattice reconstruction of $CsPbBr_3$ quantum dots, leading to a rapid increase in the density of non-radiative recombination centers, which in turn causes a sharp drop in PL intensity; while the $CsPbBr_3$@NUS-8 composite can still maintain about 72% of the initial PL intensity after 168 hours, indicating that this composite structure can greatly improve the ultraviolet resistance stability of the material. Figures 5c and 5d summarize the PL intensity retention rates of the two materials under air, high humidity (relative humidity 65%) and ultraviolet irradiation conditions in the form of bar chart and radar chart respectively. Under all test conditions, the PL retention rate of the $CsPbBr_3$@NUS-8 composite is better, confirming that the synergistic effect of structural confinement and interface stability can improve the long-term emission durability of the material.

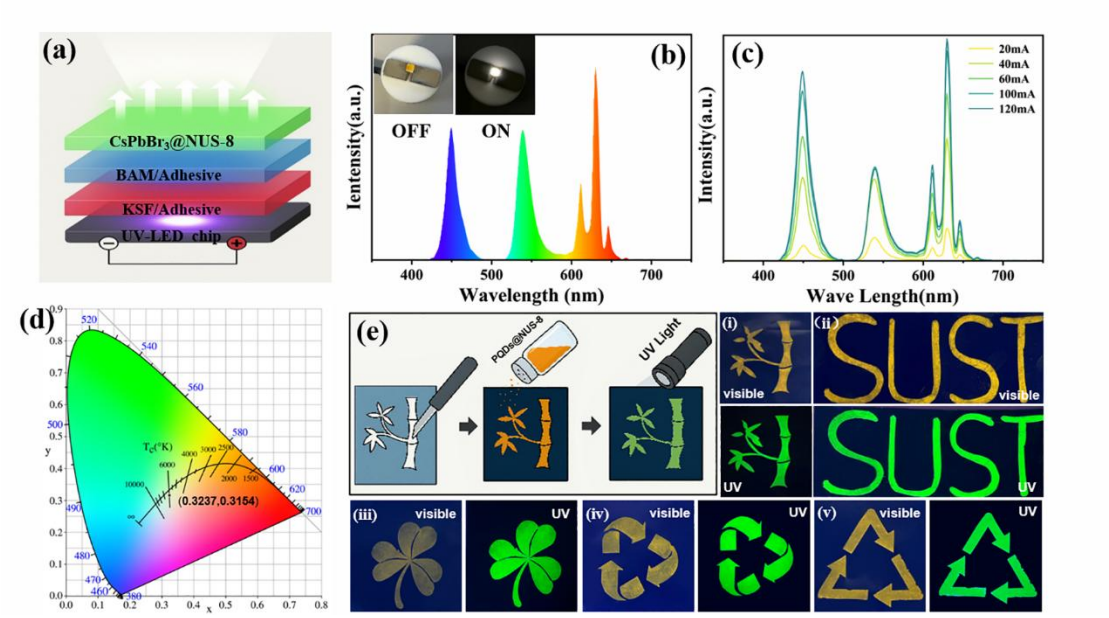


Figure 6. (a) Schematic structure of a WLED device fabricated using $CsPbBr_3$@NUS-8 composite powder as the emissive layer; (b) electroluminescence (EL) spectrum of the $CsPbBr_3$@NUS-8-based WLED (inset: photographs of the device in the off and on states); (c) EL spectra of the WLED under different driving currents (20, 40, 60, 100 and 120 mA); (d) CIE chromaticity diagram of the $CsPbBr_3$@NUS-8-based WLED and the corresponding chromaticity coordinate position; (e) schematic illustration of fluorescent patterns prepared from $CsPbBr_3$@NUS-8 composite powder and photographs under visible light and 365 nm UV irradiation, including the “SUST” lettering and comparative displays of different patterns (e.g., clover and recycling symbol).

To explore the applicability of $CsPbBr_3$@NUS-8 composite in the field of LED lighting, a WLED was prepared using $CsPbBr_3$@NUS-8 composite powder as the color conversion layer. As shown in Figure 6a, the composite powder and UV curable resin are mixed at a mass ratio of 1:1, then deposited on the blue/red conversion layer composed of commercial blue phosphor ($BaMgAl_{10}O_{17}:Eu^{2+}$) and red phosphor ($K_2SiF_6:Mn^{4+}$), and then the obtained phosphor-resin mixture is coated on a 365 nm UV LED chip to obtain the $CsPbBr_3$@NUS-8 WLED. Figure 6b shows the electroluminescence (EL) spectrum of this WLED at a working current of 40 mA. The three peaks correspond to the characteristic emission bands of the three luminescent components respectively. The inset shows the optical photos of the WLED device in off and on states at a driving current of 40 mA. As can be seen from Figure 6b, the device emits bright white light with high color saturation after being turned on. Figure 6c shows the changes of emission spectra under different currents (20, 40, 60, 100 and 120 mA). It can be seen that the emission intensities of all wavelengths increase synchronously with the increase of current, the peak shape hardly changes, and the spectral distribution remains stable, indicating that there is no emission saturation phenomenon, which further confirms the excellent stability of the composite. The chromaticity coordinate of this WLED is (0.3237, 0.3154), which is close to the standard white point (0.33, 0.33) (Figure 6d). In addition, as shown in Figure S10, the color gamut of this device can reach 126.1% of the National Television Systems Committee (NTSC) standard, which meets the requirements of lighting applications, highlighting the application potential of $CsPbBr_3$@NUS-8 in the field of LED devices.

In addition, as shown in Figure 6e, the patterned deposition of $CsPbBr_3$@NUS-8 composite powder on substrates such as wallpaper can be realized by adopting the "sand painting" patterning strategy. Specifically, first, the surface of the wallpaper is mechanically engraved to carve out the preset pattern area, and then the $CsPbBr_3$@NUS-8 powder is evenly sprinkled on the pre-engraved area to obtain a visible pattern. The obtained pattern is orange-yellow under visible light, and emits strong green fluorescence with clear boundaries under 365 nm ultraviolet excitation. As shown in Figure 6e(ii), the pattern with the abbreviation "SUST" (the English abbreviation of Shaanxi University of Science and Technology) emits clear and bright green light under ultraviolet light. In addition, other patterns such as bamboo (i), clover (iii), recycling sign (iv, v), leaves, and evacuation route signs (Figure S11) have also been successfully prepared. The above results show that this material can be used as luminescent ink to prepare high-resolution and high-contrast fluorescent patterns, which further highlights its application potential in the fields of fluorescent labeling and anti-counterfeiting.

3. Conclusion

In summary, in this study, the carboxyl-rich NUS-8 framework was used as a multifunctional confined nanoreactor, and $CsPbBr_3$ quantum dots confined in the NUS-8 framework were successfully prepared through a mechanochemical strategy. The mesoporous structure of NUS-8 can provide effective

spatial confinement for $CsPbBr_3$ perovskite quantum dots, realize the controllable growth of nanocrystals and inhibit particle agglomeration. Meanwhile, the abundant carboxyl groups in NUS-8 can coordinate with the undercoordinated Pb^{2+} sites on the surface of quantum dots, thereby passivating surface defects, reducing non-radiative recombination, and prolonging the average photoluminescence lifetime to 170.9 ns. Under the optimized conditions that the CsBr precursor ratio is 1:1 and the NUS-8 loading is 100%, the PLQY of the composite can reach 55%. Benefiting from the synergistic effect of pore confinement and defect passivation, $CsPbBr_3$@NUS-8 still retains about 85% of the initial PL intensity after being placed in air for 50 days, and the retention rate is 72% after 168 hours of continuous ultraviolet irradiation, and both environmental stability and photostability are significantly improved. In addition, this composite can be successfully applied to white light emitting diodes. The CIE coordinate of the obtained device is (0.3237, 0.3154), and the color gamut reaches 126.1% NTSC. It can also be used to prepare high-contrast fluorescent patterns, and has application potential in the field of anti-counterfeiting. This study proposes a multifunctional MOF-based strategy, which can simultaneously regulate the growth and interfacial defect chemistry of $CsPbBr_3$ quantum dots by integrating spatial confinement and chemical coordination effects.

Declaration of competing interest

The authors declare that they have no known competing financial interests or personal relationships that could have appeared to influence the work reported in this paper.

Supporting Information

Supplementary data to this article can be found online at https://doi.org/10.1016/xxxxxx.

Acknowledgements

This work was financially supported by the National Natural Science Foundation of China (Program22409127)，Young Elite Scientists Sponsorship Program by Cast，No.YESS20230159

References

1 Fakharuddin, A. *et al.* Perovskite light-emitting diodes. *Nature Electronics* **5**, 203-216 (2022).

2 Wu, X.-g. *et al.* In Situ Fabricated Perovskite Quantum Dots: From Materials to Applications. *Advanced Materials* **37**, 2412276 (2025).

3 Wang, W. *et al.* Encapsulation of perovskite quantum dots in CAU-17 organic frameworks for stable photocatalysis. *Chemical Communications* **61**, 3712-3715 (2025).

4 Zhang, J. *et al.* Encapsulating Halide Perovskite Quantum Dots in Metal–Organic Frameworks for Efficient Photocatalytic CO_2 Reduction. *Catalysts* **14**, 590 (2024).

5 Wang, X. *et al.* Encapsulating perovskite quantum dots into 3D COF for visible light-driven CO2 reduction. *Science China Chemistry* **68**, 1478-1485 (2025).

6 Aftab, S. *et al.* Perovskite Quantum Dots: Fabrication, Degradation, and Enhanced Performance Across Solar Cells, Optoelectronics, and Quantum Technologies. *Carbon Energy* **7**, 70018 (2025).

7 Sun, W. *et al.* Ligands in Lead Halide Perovskite Nanocrystals: From Synthesis to Optoelectronic Applications. *Small* **19**, 2205950 (2023).

8 Wang, Y. & Sun, H. All-Inorganic Metal Halide Perovskite Nanostructures: From Photophysics to

Light-Emitting Applications. *Small Methods* **2**, 1700252 (2018).
9 Ma, H. *et al.* Water-induced degradation mechanism of metal halide perovskite nanocrystals. *Matter* **8** (2025).
10 Tian, T. *et al.* Large-area waterproof and durable perovskite luminescent textiles. *Nature Communications* **14**, 234 (2023).
11 Song, S. *et al.* Surface Modification Strategy Synthesized CsPbX3 Perovskite Quantum Dots with Excellent Stability and Optical Properties in Water. *Advanced Functional Materials* **33**, 2300493 (2023).
12 Wu, Y. *et al.* Strategies of Improving $CsPbX_3$ Perovskite Quantum Dots Optical Performance. **Volume 9 - 2022** (2022).
13 Gong, T. *et al.* Rare Earth-Doped Perovskite Quantum Dot Microspheres for Micro-LED Displays. *ACS Energy Letters* **10**, 5012-5019 (2025).
14 Lu, C.-H. *et al.* Doping and ion substitution in colloidal metal halide perovskite nanocrystals. *Chemical Society Reviews* **49**, 4953-5007 (2020).
15 Wu, J. *et al.* Generative Synthesis of Highly Stable Perovskite Nanocrystals via Mesoporous Silica for Full-Spectrum White LED. *Small* **21**, 2507240 (2025).
16 Zhang, X. & Yang, P. $CsPbX_3$ (X = Cl, Br, and I) Nanocrystals in Substrates toward Stable Photoluminescence: Nanoarchitectonics, Properties, and Applications. *Langmuir* **39**, 11188-11212 (2023).
17 Lv, W. *et al.* Improving the Stability of Metal Halide Perovskite Quantum Dots by Encapsulation. *Advanced Materials* **31**, 1900682 (2019).
18 Mei, E. *et al.* Modified α-Al_2O_3 wafer: Enhance the stability of perovskite quantum dots with wide colour gamut for white light-emitting diodes. *Applied Surface Science* **569**, 150964 (2021).
19 C. G, S. *et al.* Stabilization of $CsPbBr_3$ quantum dots for photocatalysis, imaging and optical sensing in water and biological medium: a review. *Journal of Materials Chemistry C* **10**, 6935-6956 (2022).
20 Luo, C. *et al.* Highly Luminescent and Ultra-Stable Perovskite Films with Excellent Self-Healing Ability for Flexible Lighting and Wide Color Gamut Displays. *Advanced Functional Materials* **32**, 2113010 (2022).
21 Lyu, B. *et al.* Pattern-Matched Polymer Ligands Toward Near-Perfect Synergistic Passivation for High-Performance and Stable Br/Cl Mixed Perovskite Light-Emitting Diodes. *Angewandte Chemie International Edition* **63**, 202408726 (2024).
22 Chen, R. *et al.* Ultralong Decay Lifetime for CsPbBr3 Perovskite Quantum Dots Glass. *Advanced Optical Materials* **13**, 01385 (2025).
23 Tsai, H. *et al.* Bright and stable light-emitting diodes made with perovskite nanocrystals stabilized in metal–organic frameworks. *Nature Photonics* **15**, 843-849 (2021).
24 Meng, G. *et al.* Confining perovskite quantum dots in the pores of a covalent-organic framework: quantum confinement- and passivation-enhanced light-harvesting and photocatalysis. *Journal of Materials Chemistry A* **9**, 24365-24373 (2021).
25 Shankar, H. *et al.* Boosting the stability of lead halide perovskite nanocrystals by metal–organic frameworks and their applications. *Journal of Materials Chemistry C* **10**, 11532-11554 (2022).
26 Wang, P. *et al.* Ultrastable Perovskite–Zeolite Composite Enabled by Encapsulation and In Situ Passivation. *Angewandte Chemie International Edition* **59**, 23100-23106 (2020).
27 Zhan, Y. *et al.* Stable and Bright $CsPbX_3$ Nanocrystals in Metal–Organic Frameworks for White Light-Emitting Diodes. *Langmuir* **38**, 11121-11129 (2022).

28 Rubino, A. *et al.* Mesoporous Matrices as Hosts for Metal Halide Perovskite Nanocrystals. *Advanced Optical Materials* **8**, 1901868 (2020).

29 Gao, C. *et al.* Enhanced photoluminescence and stability of $CsPbBr_3$ quantum dots by anchoring on metal-organic frameworks for Cu^{2+} detection fluorescence probe. *Journal of Alloys and Compounds* **1023**, 180159 (2025).

30 Guo, L. *et al.* Effect of band structure on the photocatalytic performance of $CsPbBr_3$/UiO-66 composites. *Journal of Solid State Chemistry* **339**, 124962 (2024).

31 Zhang, X. *et al.* Metal–Organic Frameworks (MOFs) and MOF-Derived Materials for Energy Storage and Conversion. *Electrochemical Energy Reviews* **2**, 29-104 (2019).

32 Ren, J. *et al.* Dual-emitting $CsPbX_3$@ZJU-28 (X = Cl, Br, I) composites with enhanced stability and unique optical properties for multifunctional applications. *Chemical Engineering Journal* **391**, 123622 (2020).

33 Lin, C.-C. *et al.* Achieving long-term water stability and strong exciton–photon coupling in $CsPbBr_3$ quantum dots via MOF encapsulation. *Nanophotonics* **14**, 2397-2409 (2025).

34 Zhao, Y. *et al.* $CsPbX_3$ Quantum Dots Embedded in Zeolitic Imidazolate Framework-8 Microparticles for Bright White Light-Emitting Devices. *ACS Applied Nano Materials* **4**, 5478-5485 (2021).

35 Ren, J. *et al.* Encapsulating all-inorganic perovskite quantum dots into mesoporous metal organic frameworks with significantly enhanced stability for optoelectronic applications. *Chemical Engineering Journal* **358**, 30-39 (2019).

36 Liu, J. *et al.* High photoluminescence quantum yield and stability achieved by encapsulating MAPbBr3 QDs in UIO-66 and their application in LEDs. *Optics Express* **32**, 36964-36975 (2024).

37 Wan, S. *et al.* Perovskite-type $CsPbBr_3$ quantum dots/UiO-66 (NH_2) nanojunction as efficient visible-light-driven photocatalyst for CO_2 reduction. *Chemical Engineering Journal* **358**, 1287-1295 (2019).

38 Zhang, D. *et al.* Synthesis and Luminescence Properties of $CsPbX_3$@Uio-67 Composites toward Stable Photoluminescence Convertors. *Inorganic Chemistry* **58**, 1690-1696 (2019).

39 Shankar, H. *et al.* Significant boost of the stability and PLQYof $CsPbBr_3$ NCs by Cu-BTC MOF. *Scientific Reports* **12**, 7848 (2022).

40 Yuan, H. *et al.* Large-Area Fabrication of Ultrathin Metal-Organic Framework Membranes. *Advanced Materials* **35**, 2211859 (2023).

41 Yuan, H. *et al.* Solution-Processable Metal–Organic Framework Nanosheets with Variable Functionalities. *Advanced Materials* **33**, 2101257 (2021).

42 Peng, Y. *et al.* Enhanced fluorescence and stability of CsPbBr3 perovskite nanocrystals via MOF-5 encapsulation with hierarchical pore structures. *Ceramics International* **51**, 31818-31827 (2025).

43 Svidrytski, A. *et al.* Modeling the Impact of Mesoporous Silica Microstructures on the Adsorption Hysteresis Loop. *The Journal of Physical Chemistry C* **124**, 21646-21655 (2020).

44 Thommes, M. *et al.* Physisorption of gases, with special reference to the evaluation of surface area and pore size distribution (IUPAC Technical Report). **87**, 1051-1069 (2015).

45 Jones, C. M. S. *et al.* Optimized photoluminescence quantum yield in upconversion composites considering the scattering, inner-filter effects, thickness, self-absorption, and temperature. *Scientific Reports* **11**, 13910 (2021).

46 Lian, Z.-D. *et al.* Highly Stable $CsPbBr_3$ Perovskite Nanocrystals Encapsulated in Metal–Organic Frameworks for White Light-Emitting Diodes. *ACS Applied Nano Materials* **6**, 1808-1816 (2023).

Supplementary Files

This is a list of supplementary files associated with this preprint. Click to download.

- supportting.docx